RSC Advances

PAPER

View Article Online
View Journal | View Issue

Cite this: *RSC Adv.*, 2023, **13**, 33826

Synthesis, biological evaluation and *in silico* investigations of benzotriazole derivatives as potential inhibitors of NIMA related kinase†

Tahir Qadri,‡[a] Mubashir Aziz,‡[b] Pervaiz Ali Channar,[c] Syeda Abida Ejaz, *[b] Mumtaz Hussain,[a] Hafiz Muhammad Attaullah,[b] Rabail Ujan,[d] Zahid Hussain,*[a] Tasneem Zehra,[c] Aamer Saeed,[e] M. R. Shah,[f] Hanan A. Ogaly [g] and Fatimah A. M. Al-Zahrani[g]

In the current study, a novel compound, bis(3-(2*H*-benzo[*d*][1,2,3]triazol-2-yl)-2-(prop-2-yn-1-yloxy)-5-(2,4,4-trimethylpentan-2-yl)phenyl)methane (TAJ1), has been synthesized by the reaction of 6,6′-methylenebis(2-(2*H*-benzo[*d*][1,2,3]triazol-2-yl)-4-(2,4,4-trimethylpentan-2-yl)phenol) (1), propargyl bromide (2) and potassium carbonate. Spectroscopic (FTIR, ^{1}H-NMR, ^{13}C-NMR) and single-crystal assays proved the structure of the synthesized sample. XRD analysis confirmed the structure of the synthesized compound, showing that it possesses two aromatic parts linked *via* a $-CH_2$ carbon with a bond angle of 108.40°. The cell line activity reported a percent growth reduction for different cell types (HeLa cells, MCF-7 cells, and Vero cells) under various treatment conditions (TAJ1, cisplatin, and doxorubicin) after 24 hours and 48 hours. The percent growth reduction represents a decrease in cell growth compared to a control condition. Furthermore, density functional theory (DFT) calculations were utilized to examine the frontier molecular orbitals (FMOs) and overall chemical reactivity descriptors of TAJ1. The molecule's chemical reactivity and stability were assessed by determining the HOMO–LUMO energy gap. TAJ1 displayed a HOMO energy level of −0.224 eV, a LUMO energy level of −0.065 eV, and a HOMO–LUMO gap of 0.159 eV. Additionally, molecular docking analysis was performed to assess the binding affinities of TAJ1 with various proteins. The compound TAJ1 showed potent interactions with NEK2, exhibiting −10.5 kcal mol^{-1} binding energy. Although TAJ1 has demonstrated interactions with NEK7, NEK9, TP53, NF-KAPPA-B, and caspase-3 proteins, suggesting its potential as a therapeutic agent, it is important to evaluate the conformational stability of the protein–ligand complex. Hence, molecular dynamics simulations were conducted to assess this stability. To analyze the complex, root mean square deviation (RMSD) and root mean square fluctuation analyses were performed. The results of these analyses indicate that the top hits obtained from the virtual screening possess the ability to act as effective NEK2 inhibitors. Therefore, further investigation of the inhibitory potential of these identified compounds using *in vitro* and *in vivo* approaches is recommended.

Received 9th September 2023
Accepted 6th November 2023

DOI: 10.1039/d3ra06149c

rsc.li/rsc-advances

Introduction

In all ages, cancer remains the major health problem worldwide, and is characterized by abnormal, uncontrolled and rapid proliferation of malignant tissues or cells.[1] According to Cancer Research UK, it is estimated that there were 18.1 million new cases of cancer all over the world in 2020,[2] which imposes the largest disease burden affecting the quality of life in both men and women. Among all types of cancer, breast cancer is a potential type of cancer relating to death in women.[3] Normally the cell cycle is controlled by several endogenous factors, including different NIMA-related kinases (NEK).[4] In previous

[a]*Department of Chemistry, University of Karachi, Karachi 75270, Pakistan. E-mail: zahidhussain@uok.edu.pk*

[b]*Department of Pharmaceutical Chemistry, Faculty of Pharmacy, The Islamia University of Bahawalpur, Bahawalpur 63100, Pakistan. E-mail: abida.ejaz@iub.edu.pk*

[c]*Department of Basic Science and Humanities, Faculty of Information Science Humanities, Dawood University of Engineering and Technology Karachi, 74800, Karachi, Pakistan*

[d]*Dr M. A. Kazi Institute of Chemistry, University of Sindh, Jamshoro, Pakistan*

[e]*Department of Chemistry, Quaid-I-Azam University, Islamabad 45320, Pakistan*

[f]*H.E.J.Research Institute of Chemistry, International Center for Chemical and Biological Sciences, University of Karachi, Karachi 7527, Pakistan*

[g]*Chemistry Department, College of Science, King Khalid University, Abha 61421, Saudi Arabia*

† Electronic supplementary information (ESI) available: NMR spectra of the synthesized compounds. CCDC 2149670. For ESI and crystallographic data in CIF or other electronic format see DOI: https://doi.org/10.1039/d3ra06149c

‡ These authors have contributed equally to this work.

studies, NEK proteins were extensively reviewed in the maintenance of mitotic events, concerned with the discovery of new anti-neoplastic drugs. Among all the NEK proteins, NEK2, NEK7 and NEK9 regulate the duplication of centrosome, protein transport, and spindle formation.[5–7] NEK2, serine/threonine protein kinase, consisting of 445 amino acids,[8] highly expressed in S and G2 phases, prevents the premature separation of the centrosome. Its absence interferes with centrosome separation in the G2 phase and causes the loss of centrosomal antigens.[9] NEK2 is highly expressed in various types of cancer, including breast cancer, and is significantly involved in cancer progression.[10] Inhibition of NEK2 protein causes growth suppression, leading to cell death, and this can be used to reduce the progression of tumor cells. So, NEK2 is considered a novel drug target for the treatment of cancer.[11]

NEK7 is a serine/threonine kinase composed of approximately 302 amino acids.[12] It is greatly expressed in S and G1 phases in various human body organs, including the lungs and liver. NEK7 is specifically linked with the duplication of the centrosome, encouraging cell division in the S0 phase which can produce cancer, and it is also involved in the occurrence and progression of various inflammatory diseases, including auto-immune disorders, Alzheimer's disease, inflammatory bowel diseases and gout.[1,13] NEK7 is a potential target for novel drugs, especially in cancer therapy. NEK9 is another NIMA-related kinase protein, considered to be the first NEK which is overexpressed in breast cancer, which interferes with the action of other NEK proteins, including NEK6 and NEK7. NEK9 catalyzes the phosphorylation and activation of NEK6 and NEK7. Moreover, NEK9 is also involved in normal centrosome segregation during cell division.[14] Inhibition of NEK9 causes abnormal mitosis and may induce the early apoptosis of cancer cells.[15] So, NEK9 is also considered a potential drug target for the development of novel anti-cancer drugs.

Several attempts have been made to identify the novel inhibitors of NIMA-related kinases. In particular, Aziz *et al.* identified selective and potential inhibitors of NEK7 kinase. However, these inhibitors were selective against a single member of the NIMA family, but the current study targets multiple NIMA kinases and cancer proteins *via* novel synthetic compounds. Previously reported 1,2,4 triazole derivatives possessing anti-cancer potential are given in Fig. 1.[16]

In the United States, there are currently 53 FDA-approved medications that exhibit anti-cancer properties, and ongoing research has identified over 200 potential candidates for the development of new anti-cancer agents. However, none of the FDA-approved inhibitors have been found to possess inhibitory effects against the NEK7 protein. This suggests a lack of currently available effective NEK7 inhibitors. The utilization of compounds with heterocyclic nuclei has garnered significant attention in the development of novel antimicrobial agents due to their therapeutic importance. Benzotriazole and its derivatives, in particular, have attracted considerable interest due to their wide range of applications, including pharmaceutical therapeutics,[17,18] corrosion-resistant materials,[19] intermediates for other synthetic materials,[20] and supramolecular ligands.[21] Benzotriazole-based compounds are a distinctive group of nitrogen-containing heterocycles that have garnered considerable interest among medicinal chemists. They are recognized as a promising class of bioactive heterocyclic product with diverse biological properties,[22] such as anti-inflammatory,[23] antiprotozoal,[24] antiproliferative,[25] anticancer,[26] antiviral,[27] plant growth regulatory[28] and antibacterial activities,[29] as shown in Fig. 2. The chemical structure of benzotriazole has been demonstrated to possess remarkable versatility in its properties. It has recently been utilized as an effective leaving group following reactions with various carbonyl groups. Additionally, it can be readily incorporated into other chemical structures through a series of reactions, including condensation and addition reactions.[30] The use of benzotriazole as a synthetic auxiliary in the benzotriazole methodology developed by Katrizsky and coworkers[31] is interesting. In one study, it was observed that benzotriazoles have the ability to form complexes with various transition metals.[32] Another study indicated that benzotriazole derivatives, when engaged in coordination complexes with transition metals, exhibit promising anticancer capabilities.[33] Benzotriazole can function as a precursor of radicals,[34] while some authors have also reported the synthesis of stable nitrenium ions using benzotriazole as a synthon.[35] The utilization of polymer-supported benzotriazoles as catalysts for the synthesis of tetrahydroquinoline through condensation reactions highlights their significant role in the realm of catalysis.[36]

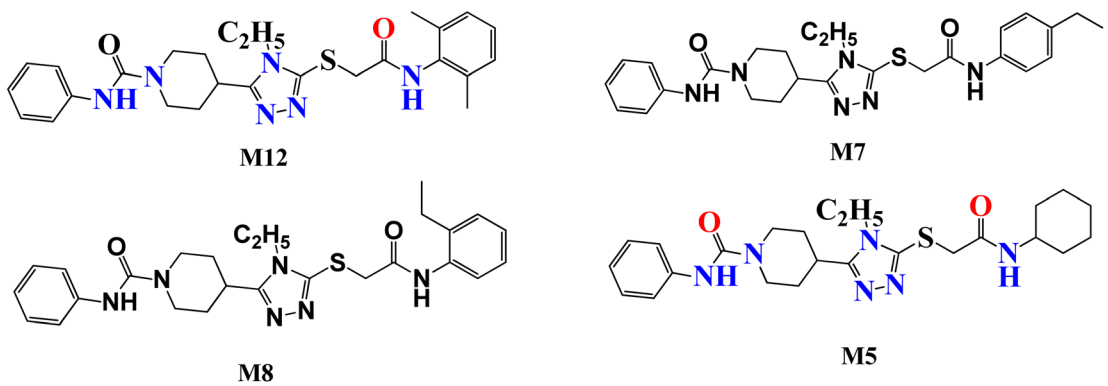

Fig. 1 Previously reported 1,2,4 triazole derivatives as a potential inhibitor of NEK7 *via in silico* studies.

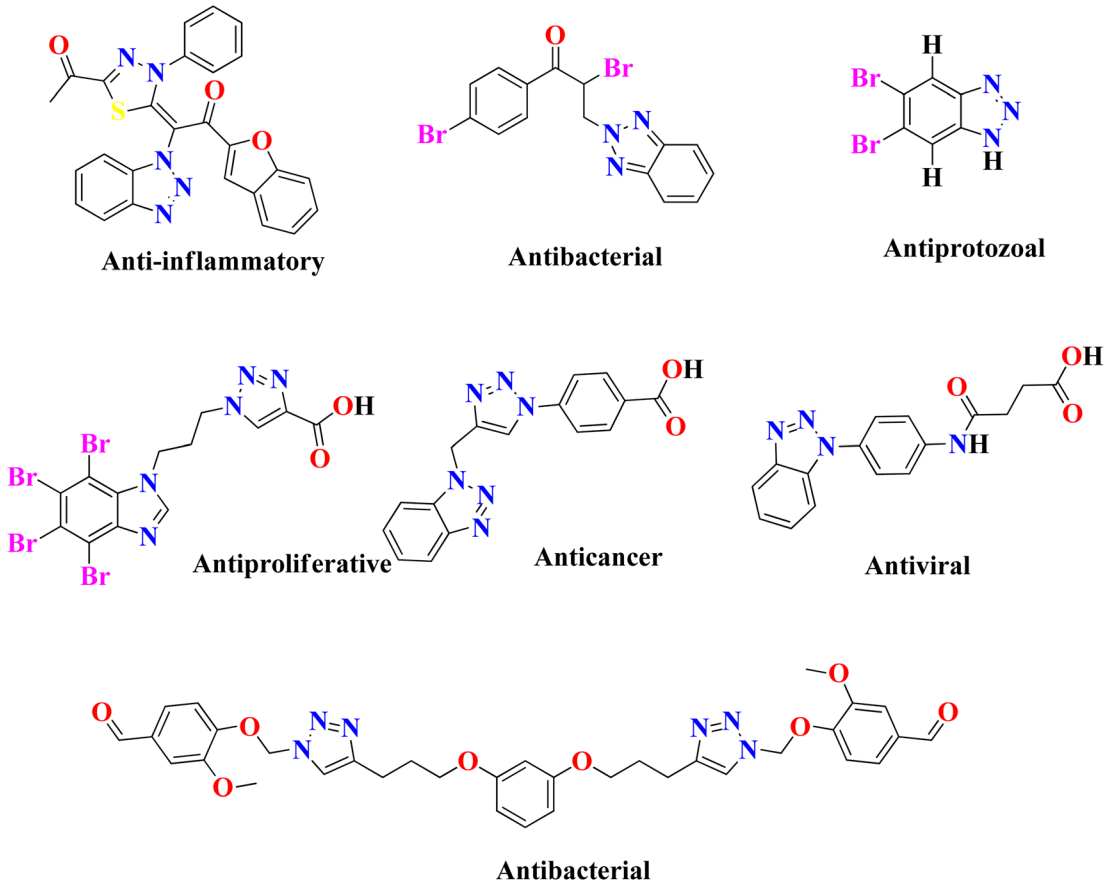

Fig. 2 Previously reported heterocyclic products that exhibit various biological properties.

Based on the properties and importance of heterocyclic compounds, there is a need to explore NEK 7 inhibitors and for this purpose, the current study is focused on a combination of experimental and computational approaches to explore bis(3-(2*H*-benzo[*d*][1,2,3]triazol-2-yl)-2-(prop-2-yn-1-yloxy)-5-(2,4,4-trimethylpentan-2-yl)phenyl)methane as a potential NEK7 inhibitor with the goal of disrupting anticancer pathways and treating breast cancer and associated malignancies.[14,16] The synthesized compound was tested against three cancer cell lines; two human breast cancer cell lines (the MDA-MB231 cell line (HTB-26™) and the MCF-7 cell line (HTB-22™)), and one human cervical cancer cell line (the HeLa cell line and CRM-CCL-2™). For *in silico* investigations, molecular docking studies (using p53, caspase, and NF-KB) and molecular dynamic simulation studies were performed followed by the density functional theory (DFT) calculations.

Experimental

Synthesis of bis(3-(2*H*-benzo[*d*][1,2,3]triazol-2-yl)-2-(prop-2-yn-1-yloxy)-5-(2,4,4-trimethyl pentan-2-yl)phenyl)methane (TAJ1)

A solution of 6,6′-methylenebis(2-(2*H*-benzo[*d*][1,2,3]triazol-2-yl)-4-(2,4,4-trimethylpentan-2-yl)phenol) (1) (100 mg, 0.152 mmol) was stirred in acetone (15 ml) with the addition of K_2CO_3 (51 mg, 0.0364 mmol) and 3-bromoprop-1-yne (0.035 ml, 0.395 mmol) in a dropwise manner. The reaction mixture was refluxed in acetone for 14 hours. The progress of the reaction was monitored by TLC until complete consumption of 6,6′-methylenebis(2-(2*H*-benzo[*d*][1,2,3]triazol-2-yl)-4-(2,4,4-trimethylpentan-2-yl)phenol) was observed. Once completed, the reaction mixture was treated three times with a mixture of dichloromethane (DCM) and water (H_2O), followed by drying with $MgSO_4$. The solvents were evaporated using a rotary evaporator, and the crude product was purified by silica gel column chromatography using a mixture of hexane and dichloromethane in an 8 : 2 ratio (v/v). This process yielded purified bis(3-(2*H*-benzo[*d*][1,2,3]triazol-2-yl)-2-(prop-2-yn-1-yloxy)-5-(2,4,4-trimethylpentan-2-yl)phenyl)methane (3) in excellent yield. The spectra (^{13}CNMR and ^{1}HNMR) of TAJ1 are given in the ESI (Fig. S5–S7).†

Characterization data of benzotriazole (TAJ1)

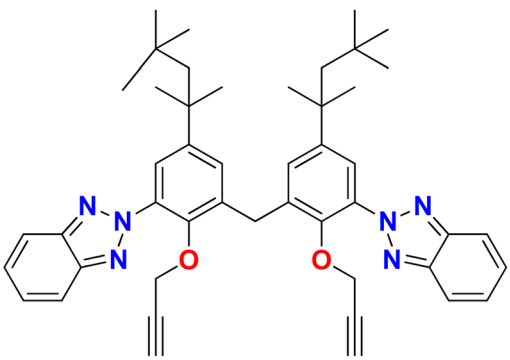

Yield; 79%, R_f: 0.41 (EtOAc : Petroleum ether 1 : 9); M. P: 250 °C; FT-IR (KBr, cm^{-1}): 3446.6 (O–H), 3300.0 (Sp-stretch), 2956.7, 2923.9 (Sp^3-CH stretch), 2854.5, 1488.9 (C=C), 997.1 ^{1}HNMR: (300 MHz, $CDCl_3$): δ 7.98 (dd, 4H, J = 6.6 Hz, 3 Hz), 7.66 (d, 2H, J = 2.4 Hz), 7.44 (dd, 4H, J = 6.6 Hz, 3.3 Hz), 7.28 (d, 2H, J = 2.1 Hz), 4.42 (s, 2H), 4.26 (d, 4H, J = 2.4 Hz), 2.26 (t, 2H, J = 2.4 Hz), 1.70 (s, 4H), 1.32 (s, 12H), 0.74 (s, 18H). EI, m/z [% rel. int.]: 734.1 [M^+, 38.6], 679.1 [84.0], 663.1 [100], 302.0 [43], 264.0 [86.3], 57.1 [16.5] Anal. Calcd. For $C_{47}H_{54}N_6O_2$: C, 76.81; H, 7.41; N, 11.43 found: C, 76.84; H, 7.42; N, 11.45 HRMS: $C_{47}H_{54}N_6O_2$+H 734.4308 Found 734.4306.

Biological activities

MTT assay (cell viability assay). To conduct anti-cancer tests, the current study evaluated the derivatives against two types of cancer cell line: HeLa (human cervical cancer) and MCF-7 (human breast cancer). The testing method used was previously described by Mosmann (1983) and Nik and Otto (1990),[37,38] which we also referenced in our previously published article.[39] The experimental procedure was conducted using 96-well flat-bottom plates. Each well was filled with 90 μL of medium and seeded with 10×10^4 cells. A test chemical solution of 100 μL was then added to each well, followed by an incubation period of 24 hours at 37 °C and 5% CO_2. Positive and negative control wells were prepared with 10 μL of a standard drug (cisplatin) and 100 μL of cell medium (without the test chemical), respectively. Subsequently, 10 μL of the MTT reagent was added to each well, and the plate was incubated for 4 hours at 37 °C. Next, 100 μL of a 10% sodium dodecyl sulfate solution was introduced, and the mixture was kept at room temperature for 30 minutes with intermittent shaking. Finally, the optical density was measured as an indicator of the results. All experiments were performed in triplicate, and the outcomes were expressed as percent growth inhibition values, as previously explained.[39]

X-ray crystal structure and refinement. The crystallographic data of the drug mentioned in the study were obtained using a Rigaku Oxford Diffraction Eos, Gemini diffractometer. Cu K radiation with a wavelength of 1.5418 Å was employed. The structures were solved and refined using the SHELX program packages[40] and the multi-scan absorption correction was applied to the collected data[41] In addition, the ORTEP-3 program was used to generate the structural drawings.[42] The positions of the hydrogen atoms in the structure were initially determined geometrically, with NH hydrogen at a distance of 0.88 Å, CH hydrogen at a distance of 0.95 Å, and CH_3 hydrogen at a distance of 0.98 Å. Subsequently, a riding model was applied to refine the positions of these hydrogen atoms, incorporating the constraints of $U_{iso}(H) = k \times U_{eq}$ (C, N), where k = 1.2 for NH and CH hydrogens, and k = 1.5 for CH_3 hydrogens. The crystallographic data for the structure discussed in this study has been deposited with the Cambridge Crystallographic Data Centre as ESI,† with the assigned CCDC no. 2149670. Interested parties can obtain copies of the data by contacting the CCDC at 12 Union Road, Cambridge CB2 1EZ, UK (fax: +44 1223 336033 or email: deposit@ccdc.cam.ac.uk), or by visiting their website at **http://www.ccdc.cam.ac.uk**.

Hirshfeld surface (HS) studies

Hirshfeld surface (HS) analysis is widely regarded as a highly reliable method for studying interactions within crystal structures.[43,44] In this study, Crystal Explorer 17.5.45 was employed to identify the intermolecular interactions present in the crystal structure of the molecule under investigation. The distances from the nearest nucleus on the inside and outside of the Hirshfeld surface were measured and denoted as d_i and d_e, respectively. Additionally, a normal contact distance, represented by D_{norm}, was used to characterize the interactions. The colors white, blue, and red were employed to represent different values of D_{norm}. The input file for this analysis was provided in CIF format, and for a more comprehensive understanding of Hirshfeld analysis, a detailed discussion can be found in the ESI (Tables S1–S2 and Fig. S1–S4†).[45]

Computational investigations

Density function theory (DFT) studies. To determine the ground-state geometries of the selected compounds, density functional theory (DFT) calculations were performed in a gas environment. DFT is a well-established and reliable computational approach for such optimization. The B3LYP functional correlation, along with a 6-31G* basis set, was utilized for optimizing the ground-state geometries. Additionally, the B3LYP/631-G*+(d,p) basis set was employed. This combination of methods and basis sets ensures accurate and reliable results.[46,47] The functional correlation quantifies the connection between two variables, indicating how changes in one variable are linked to changes in the other. The B3LYP technique was chosen for its ability to incorporate electron correlation effects effectively. Additionally, it accurately calculates various parameters, including bond angles, bond length, and infrared spectra. The B3LYP method combines the strengths of both density functional theory (DFT) and the Hartree–Fock method, resulting in a significantly enhanced representation of a molecule's electronic configuration and surpassing the precision of each approach individually.[48] In addition, selection of the basis set was based on its computational efficiency and accuracy as the 6-31G* basis set is a computationally efficient and versatile option for density functional theory (DFT) calculations. It strikes a balance between accuracy and computational cost, making it suitable for studying moderate-sized systems or when a large number of calculations are required. Despite its compact size, it includes polarization functions that effectively account for electron correlation effects, improving the precision of calculated properties. The 6-31G* basis set is widely applicable to a range of chemical systems, making it a popular choice in fields like drug discovery and materials science. It offers a practical compromise between accuracy and computational efficiency, allowing for efficient calculations without sacrificing too much accuracy. Overall, the 6-31G* basis set is a valuable tool in DFT calculations, providing a compact and versatile representation that can handle a variety of chemical systems.[48] The initial structures of the compounds were optimized using Gaussian 09w software.[49] To achieve energy minimization, the harmonic vibrational analysis was performed by excluding the

imaginary frequencies.[50] For visualization purposes, Gaussian View 6.0 was utilized.[51]

Molecular docking analysis. To analyze the interactions between the newly synthesized compounds and specific proteins, molecular docking was conducted. The 3D crystal structures of the targeted proteins, namely NEK2, NEK7, NEK9, TP53, NF-KAPPA-B P65, and caspase-3, were obtained from the Protein Data Bank (PDB) [www.rcsb.org]. The corresponding PDB IDs for the structures are 2W5A, 2WQN, 3ZKE, 3DCY, 1NFI, and 3DEI, respectively.[52] Prior to docking analysis, the proteins were prepared using MGL tools, by removing heteroatoms and water molecules followed by the addition of polar hydrogen atoms and Kollman charges. After that protein structures were rendered and corrected for missing residues.[53] The 3D structure of the synthesized compound was drawn using ChemDraw 3D.[54] To obtain the most stable arrangement of atoms energy minimization was undertaken. Docking analysis was performed with the target protein using AutoDock's default genetic algorithm as the scoring function. The use of genetic algorithms (GAs) in molecular docking studies offers several advantages, including the ability to explore a wide conformational space and handle flexible ligands and receptors. GAs are widely used and can be done in parallel for faster exploration. However, their performance is dependent on the scoring function used, and they can be computationally intensive and susceptible to local minima. Parameter tuning is also necessary for optimal results. However, genetic algorithms can provide consistent and reliable results.

The grid box dimensions for docking were set as follows: (−15.405234, 12.629904, 16.900952) for 2W5A, (−6.156441, −22.219984, −44.192549) for 2WQN, (−24.379561, −36.732107, 16.920308) for 3ZKE, (30.483200, 32.901400, −2.936000) for 3DCY, (−8.458537, 55.130635, −29.220624) for 1NFI, and (−47.297718, 9.871887, −24.212191) for 3DEI. Subsequently, the newly synthesized compound was docked into the active pocket of the target proteins, generating 100 different configurations for each protein. The configuration with the most stable structure and the lowest binding energy was selected for further analysis. The interactions formed between the synthesized compound and the targeted proteins were then explored in both 2D and 3D positions. The outcomes of this study aim to facilitate the design of novel compounds with improved binding affinities to the target proteins.

Molecular dynamic simulations. Molecular dynamic (MD) simulation is a computational tool for the analysis of molecular interactions of docked complexes as a function of time.[55] In the current study, Nanoscale Molecular Dynamics (NAMD) software 1.9.3 was employed for the prediction of the dynamic nature of the protein–ligand complex. The complex possessing the best binding energy from molecular docking results was selected for MD simulation. The topology files for simulations were generated by CHARM-GUI.[56] All molecules including ligand and proteins were described using CHARMM36 force field parameters under periodic boundary conditions. Normal physiological conditions were selected by solvating the molecules with water (TIP3P), and counter ions including NaCl (0.15 M) were added to neutralize the simulation box. Prior to simulation, the system was equilibrated in NVT and NPT ensembles with a Berenson thermostat and barostat for 2 fs at 300 K. The RMSD and RMSF were calculated using VMD 1.9.3 by the Ewald summation method.[57] Finally, MD simulations were tracked for 50 ns.

Results and discussion

Chemistry

Synthesis of bis(3-(2*H*-benzo[*d*][1,2,3]triazol-2-yl)-2-(prop-2-yn-1-yloxy)-5-(2,4,4-trimethylpentan-2-yl)phenyl)methane (TAJ1). TAJ1 was prepared by reacting 6,6′-methylenebis(2-(2*H*-benzo[*d*][1,2,3]triazol-2-yl)-4-(2,4,4-trimethylpentan-2-yl) phenol) (1) with propargyl bromide (2) along with K_2CO_3 that was used as base for deprotonation. The reaction was kept under stirring at 70 °C for 18 hours. After cooling the reaction mixture (a well-known procedure), as shown in Scheme 1, the synthesized analogue (3) was characterized by various techniques, such as IR, NMR and HPLC-MS, ^{1}H NMR and ^{13}C NMR. The ^{1}HNMR spectrum revealed all the expected signals, as two singlets were seen at δ 0.74 ppm and δ 1.32 ppm with the integration of eighteen and twelve methyl protons. Methylene protons of the alkyl group region were exposed as a singlet at δ 1.70 ppm. Propargyl protons emerged at δ 2.26 ppm as a triplet with $J = 2.4$ Hz while the methylene protons attached next to the propargyl group were observed as a doublet at δ 4.26 ppm with the integration of 4H and a J value equal to 2.4 Hz. Methylene protons present at the symmetry point and joining the two parts of this molecule were exposed as a singlet at δ 4.42 ppm. The aromatic region was also fruitful as per the requirement, which

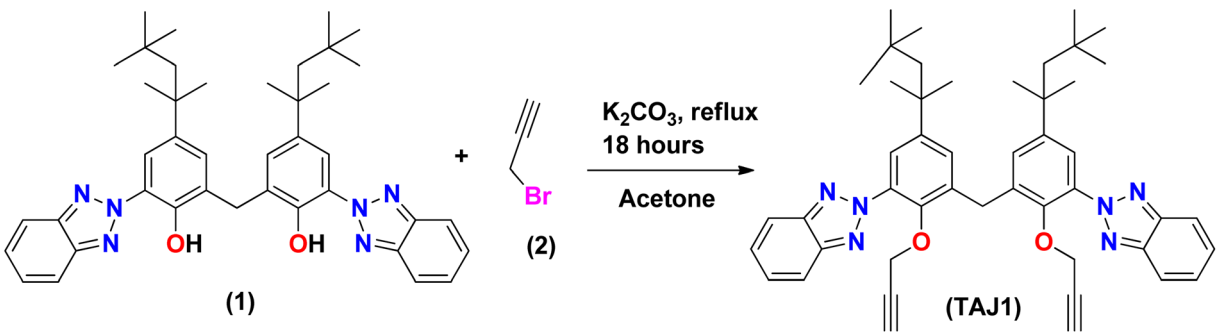

Scheme 1 Synthesis of bis(3-(2*H*-benzo[*d*][1,2,3]triazol-2-yl)-2-(prop-2-yn-1-yloxy)-5-(2,4,4-trimethyl pentan-2-yl)phenyl)methane (TAJ1).

was exposed a doublet at δ 7.28 ppm with the coupling constant $J = 2.1$ Hz for 2H. A signal δ 7.44 ppm was revealed as a doublet of doublets with J values 6.6 and 3.3 Hz which was integrated as 4H. Another doublet was observed at δ 7.66 ppm with the coupling constant $J = 2.4$ Hz for 2H. Lastly, we observed a doublet of doublet at δ 7.98 ppm with J values 6.6 and 3 Hz for four protons. The mass spectrum was found to be same as that calculated from the chemical formula, since it showed M^+ at m/z 734.1 while fragmentation produced the following ions. A fragment observed at m/z 679.1 was formed by the removal of the tertiary butyl group from the molecule. A base peak was seen at m/z 663.1 which came into existence because of the elimination of a methyl group and the production of a tertiary carbocation. A fragment also emerged at m/z 264.0 due to the exclusion of an alkyl group from compound (3). A peak at 3300 cm^{-1} was observed in the infrared spectrum of the C–H stretch of terminal alkynes. The aromatic C–H stretch appeared at 2923.9 cm^{-1}, while the C–H stretch for alkane emerged at 2854.5 cm^{-1}. C–C stretches (in the ring) were exposed at 1488.9 cm^{-1} as well as 1460 cm^{-1}, whereas the C–N stretch was captured at 1267.1 cm^{-1}. In aromatic C–H the "loop" was exposed at 744.5 cm^{-1}. The XRD technique also confirmed the structure. Propargyl-substituted bisphenol **3**, possess two aromatic parts linked *via* a $-CH_2$-carbon along with bond angle 108.40(13)°. The results show that the molecules interact through hydrogen bonds as C–H···N, and are responsible for the building of an extended chain parallel to the axis.[58] Hence all the afforded results confirm the synthesis of compound (3).

Cell viability assay. An MTT assay was performed to assess the effect of TAJ1 on cell viability in human breast cancer cells. As shown in Table 1, compound TAJ1 was treated with different cell lines, including HeLa cells, MCF cells and normal Vero cells. The percentage of growth reduction was analyzed. After 24 h 29% and after 48 h 14.4% HeLa cells were found to be viable. The results were very convincing in the case of MCF cells, as only 6.67% cells remain viable after 48 h. Moreover, 91.9% of normal Vero cells remain viable after 48 h. These findings suggested that TAJ1 exhibits cytotoxic effects on HeLa cells and MCF-7 cells, while it exhibits the least effect on normal Vero cells compared to previously reported anticancer cisplatin and doxorubicin drugs, as shown in Table 1. The decrease in cell viability observed with TAJ1 treatment supports its potential as an anti-cancer agent. Further studies are necessary to elucidate the underlying mechanism of action and evaluate its efficacy *in vivo*.

Table 2 Values for the GI_{50} for HeLa and MCF-7 cells

	$GI_{50} \pm$ SEM	
Code	HeLa	MCF-7
TAJ1	6.08 ± 0.16	4.04 ± 0.17
Cisplatin	2.64 ± 0.13	4.63 ± 0.21
Doxorubicin	4.21 ± 0.22	7.32 ± 0.81

The results in Table 2 reveal a distinct difference in the sensitivity of MCF-cells and HeLa-cells to TAJ1. These findings suggested that TAJ1 exhibits greater efficacy in inhibiting the growth of MCF cells compared to HeLa cells. The discrepancy in sensitivity can be attributed to innate biological differences between the cell lines, with HeLa cells originating from cervical cancer and MCF cells from breast cancer. Different cancer types have unique genetic and biochemical characteristics, resulting in variations in drug response. In the case of MCF-7 cells and HeLa cells, the 4.04 ± 0.17 and 6.08 ± 0.16 experimental values for GI_{50} might reflect variations in signaling pathways between MCF and HeLa cells, respectively. However, the lower GI_{50} value for MCF-7 cells suggests that synthesized compound TAJ1 exhibits a strong potential for tumor suppression and breast cancer treatment. These results were further validated by *in silico* studies.

In silico investigations

Density functional theory (DFT). The electronic properties were calculated and geometries of TAJ1 and previously reported inhibitors were optimized using DFT studies. In addition, the current study reports the HOMO–LUMO analysis using a DFT/631-G* and B3LYP/631-G*+(d,p) calculation setup, as shown in Table 3. The synthesized derivatives reached stability after steepest energy descents of −2604.954 hartree and −2302.373 hartree, respectively.

The HOMO and LUMO highest occupied and lowest unoccupied molecular orbitals are very decisive in a molecule. The HOMO/LUMO energy gap is the energy difference between the highest occupied molecular orbital (HOMO) and the lowest unoccupied molecular orbital (LUMO) of a molecule. A low HOMO/LUMO energy gap indicates less energy required to promote an electron from the HOMO to the LUMO, resulting in higher reactivity, visible light absorption in conjugated systems, and a harder molecule. On the other hand, a high HOMO/LUMO energy gap indicates greater energy required for

Table 1 Values for the % growth reduction after 24 and 48 hours for HeLa and MCF-7 cells

	% Growth reduction					
	HeLa Cells		MCF-7 Cells		Vero cells	
Code	After 24 h	After 48 h	After 24 h	After 48 h	After 24 h	After 48 h
TAJ1	70.1 ± 1.23	85.6 ± 2.81	68.3 ± 0.88	93.3 ± 1.66	5.03 ± 0.22	8.13 ± 0.67
Cisplatin	79.2 ± 1.44	89.1 ± 2.44	85.2 ± 2.11	98.2 ± 1.34	7.13 ± 0.54	12.1 ± 1.04
Doxorubicin	69.2 ± 1.98	82.2 ± 2.08	8.2 ± 0.69	8.6 ± 1.06	10.3 ± 0.89	15.4 ± 1.91

Table 3 Optimization energies, HOMO and LUMO energies and their gap calculated in the gas phase

Code	Optimization energy (hartree)	Dipole moment (debye)	Polarizability (α)	HOMO (eV)	LUMO (eV)	HOMO–LUMO (ΔeV)	Calculation method
TAJ1	−2604.954	2.419	573.234	−0.224	−0.065	0.159	B3LYP/631-G[a]
TAJ1	−2302.373	1.987	635.652	−0.235	−0.069	0.166	B3LYP/631-G[a]+(d,p)
M7	−1922.34	3.212	400.21	−0.220	−0.027	0.193	B3LYP/631-G[a]+(d,p)
M7[a16]	−1881.07	3.7622	350.22	−0.218	−0.023	0.194	B3LYP/SVP

[a] Previously reported parameters of compound M7.[16]

electron transfer, leading to lower reactivity, UV light absorption, and a softer molecule. The HOMO/LUMO energy gap of −0.159 eV (at B3LYP/631-G*) indicates efficient electron transfer from the molecule. In addition, it was notable that the benzene ring was localized with the LUMO orbital, whereas the triazole ring was localized with the HOMO orbitals. These regions correspond to gain and loss of electrons. Moreover, a low HOMO/LUMO energy gap for a molecule has implications for protein binding and the formation of biocomplexes. The alignment of a molecule's HOMO/LUMO energy levels with the binding site of a protein can influence its ability to interact and bind to the protein. A suitable energy gap can facilitate favorable interactions, such as the hydrogen bonding or electrostatic interactions, leading to stable protein–ligand complexes. Additionally, the HOMO/LUMO energy gap can affect the formation of biocomplexes, where molecules with an appropriate energy gap may have a greater likelihood of forming stable complexes with biological macromolecules like proteins or nucleic acids. While the HOMO/LUMO energy gap is just one factor among many that influence protein binding and biocomplex formation, understanding its impact can contribute to our understanding of molecular interactions in biological systems. The optimized structures and HOMO, LUMO orbitals are shown in Fig. 3.

Global chemical reactivity descriptors. The current study has calculated the following parameters using the HOMO (highest occupied molecular orbital) and LUMO (lowest unoccupied molecular orbital) energy values, applying their respective formulas:

$$\text{Hardness } (\eta): \eta = (E_{\text{LUMO}} - E_{\text{HOMO}})/2$$

$$\text{Softness } (S): S = 1/(2\eta)$$

$$\text{Electronegativity } (\chi): \chi = -(E_{\text{LUMO}} + E_{\text{HOMO}})/2$$

$$\text{Chemical potential } (\mu): \mu = -\chi$$

$$\text{Electrophilicity index } (\omega): \omega = \mu/(2\eta)$$

Hardness (η) indicates the reactivity and stability of a chemical system. Electronegativity (χ) represents the ability to attract electrons towards it. The electrophilicity index (ω) gauges the capacity of a molecule to accept electrons, employing the

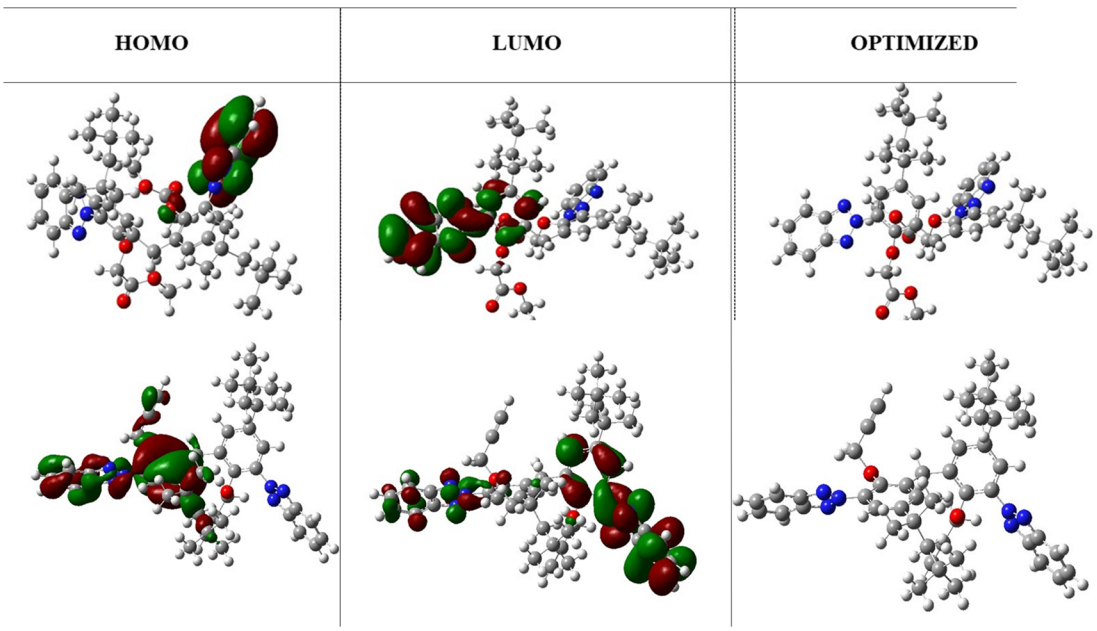

Fig. 3 The HOMO/LUMO orbitals and optimized structure of TAJ1 calculated at B3LYP/631-G* and B3LYP/631-G*+(d,p) levels of theory.

Table 4 Global reactivity descriptors of compound TAJ1

Code	Chemical potential μ (eV)	Electronegativity X (eV)	Hardness η (eV)	Softness S (eV^{-1})	Electrophilicity index ω (eV)	Calculation method
TAJ1	−0.145	0.145	0.080	6.289	0.131	B3LYP/631-G[a]
TAJ1	−0.152	0.152	0.083	6.024	0.139	B3LYP/631-G[a]+(d,p)
M7	−0.211	0.211	0.099	5.76	0.054	B3LYP/631-G[a]+(d,p)
M7[a16]	−0.121	0.121	0.097	5.135	0.075	B3LYP/SVP

[a] Previously reported parameters of compound M7.[16]

chemical potential and chemical hardness. Table 4 shows global reactivity descriptors for compound TAJ1 and a previously reported inhibitor using the proposed level of theory. The hardness value of compound TAJ1 shows the reactivity and stability of this compound. Compound TAJ1 has an electronegativity of 0.145 (at B3LYP/631-G*), which shows that it has the highest power to attract electrons towards it. Compound TAJ1 is a soft compound and it has a high electrophilicity index, which shows the power of a molecule to accept electrons with the help of chemical potential. The findings of the TAJ1 compound were correlated with already-reported triazole derivatives,[16] in which the same parameters for all triazole derivatives were estimated and the properties for one of the derivatives, *i.e.*, M7, is provided in the manuscript.

Molecular docking analysis. Molecular docking is an important computational method that predicts the binding interaction of a ligand within the active pocket of the targeted protein. The current analysis aimed to analyze the binding affinities of the synthesized compound with six distinct proteins, namely NEK2, NEK7, NEK9, TP53, NF-KAPPA-B, and caspase-3. To perform the molecular docking, we obtained the PDB IDs of the target proteins, namely 2W5A (resolution 1.55 Å) for NRK2, 2WQN (resolution 2.30 Å) for NEK7, 3ZKE (resolution 2.20 Å) for NEK9, 3DCY (resolution 1.75 Å) for TP53, 1NFI (resolution 2.7 Å) for NF-KAPPA-B P65, and 3DEI (resolution 2.80 Å) for caspase-3, from the Protein Data Bank. The detailed molecular interactions of TAJ1 against the respective protein are tabulated in Table 5.

Docking analysis revealed a potent interaction between bis(3-(2*H*-benzo[*d*][1,2,3]triazol-2-yl)-2-(prop-2-yn-1-yloxy)-5-(2,4,4-trimethylpentan-2-yl)phenyl)methane(3) and NEK2 with binding energy −10.5 kJ mol^{-1}, as given in Table 5. The TAJ1 scaffolds were involved in hydrophobic and hydrogen bonding interactions. This shows that the newly synthesized derivative may have the potential to serve as a novel therapeutic agent. The results were found to correlate with experimental investigations.

Molecular interactions analysis shows that the synthesized derivative can be a potent NEK2 inhibitor by targeting specific binding site amino acids. Compound TAJ1 demonstrates a strong binding affinity with a docking score of −10.5 kcal-mol^{-1}. It forms hydrogen bonds with TYR181 and THR179 residues and engages in hydrophobic interactions (pi-anion, pi-alkyl and alkyl) with TYR182, PRO144, LEU142, MET183, PRO180, ASP141, and LYS143 residues. On the other hand, dabrafenib exhibits a relatively weaker binding affinity with a docking score of −7.6 kcal mol^{-1}. It forms hydrogen bonds with ASN245 and THR249 residues and interacts hydrophobically with GLU246, ARG235, and PHE233 residues. These insights into the docking scores, hydrogen bonding residues,

Table 5 Molecular docking scores of compound TAJ1 against targeted proteins

Protein	PDB ID	Compound	Docking score kcal mol^{-1}	Hydrogen boning residue	Hydrophobic interactions
NEK2	2W5A	TAJ1	−10.5	TYR181, THR179	TYR182, PRO144, LEU142, MET183, PRO180, ASP141, LYS143
		Dabrafenib[a]	−7.6	ASN245, THR249	GLU246, ARG235, PHE233
NEK7	2WQN	TAJ1	−8.0	No	ASP115, ARG121, LYS63, SER46, VAL48, PHE168, ALA165
		Dabrafenib[a]	−8.3	ASP118, ARG121, GLU112, ASP179, ALA114	ALA165, PHE168, ALA61
NEK9	3ZKE	TAJ1	−5.7	No	ALA39, LYS36, PHE62, ILE57, ARG60
		Dabrafenib[a]	−0.0	No	No
TP53	3DCY	TAJ1	−9.5	ARG203	TYR92, LEU125, ALA200, PRO115, ARG10, THR230, PRO231, VAL229
		Dabrafenib[a]	−0.7	No	No
NF-KAPPA-B	1NFI	TAJ1	−8.8	No	VAL97, PHE103, LEU89, VAL93, ARG166, GLU103, PHE77, PRO69
		Dabrafenib[a]	−8.4	THR164, ARG174	No
Caspase-3	3DEI	TAJ1	−7.3	No	TRP206, TRY204, LEU168, PHE256
		Dabrafenib[a]	−5.5	LYS138, ASP146, ARG147	No

[a] The previously reported NEK7 inhibitor[1] was used as a reference standard.

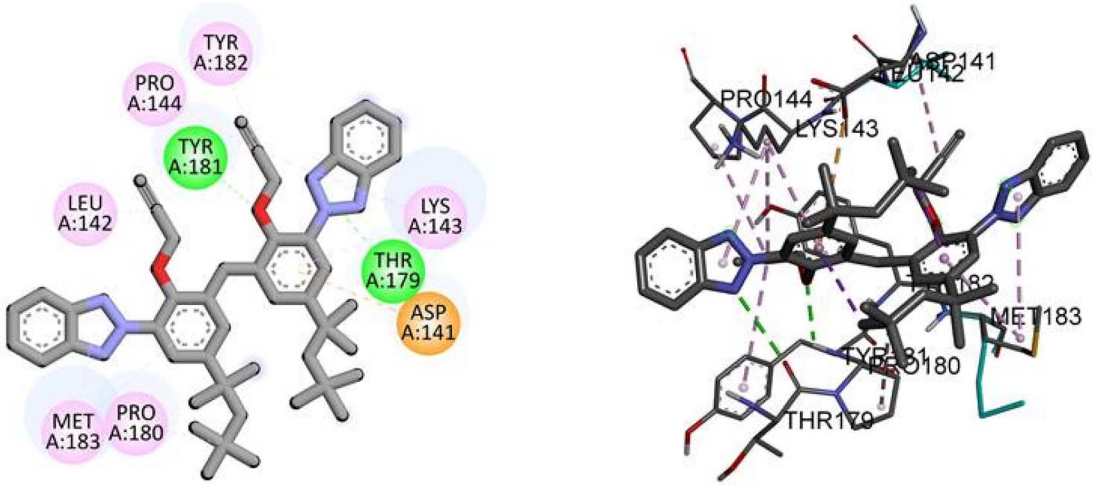

Fig. 4 The predicted 2D and 3D binding modes of TAJ1 against NEK2.

and hydrophobic interactions provide valuable information about the potential binding modes and interactions of these compounds with the target protein, as shown in Fig. 4.

Compound TAJ1 demonstrates a moderate binding affinity with a docking score of −8.0 kcal mol^{-1}. No specific hydrogen bonding residues are mentioned, but it engages in hydrophobic interactions with ASP115, ARG121, LYS63, SER46, VAL48, PHE168, and ALA165 residues. On the other hand, dabrafenib shows a relatively stronger binding affinity with a docking score of −8.3 kcal mol^{-1}. It forms hydrogen bonds with ASP118, ARG121, GLU112, ASP179, and ALA114 residues, and interacts hydrophobically with ALA165, PHE168, and ALA61 residues. These findings provide insights into the potential binding modes and interactions of NEK7 and dabrafenib with the target protein. Fig. 5 illustrates the presumed 2D and 3D binding modes of compound TAJ1 against NEK7.

Similarly, the docking results for NEK9 and dabrafenib reveal interesting findings. NEK9 exhibits a moderate docking score of −5.7 kcal mol^{-1}, indicating a potential binding affinity with the target protein. However, no specific hydrogen bonding residues are mentioned for NEK9. Instead, it engages in hydrophobic interactions with ALA39, LYS36, PHE62, ILE57, and ARG60 residues. On the other hand, dabrafenib demonstrates a docking score of −0.0 kcal mol^{-1}, suggesting a lack of binding affinity with the target protein. No hydrogen bonding residues or hydrophobic interactions are reported for dabrafenib. These results highlight the differences in binding potentials between NEK9 and dabrafenib, with NEK9 showing a moderate affinity through hydrophobic interactions, while dabrafenib appears to have no specific binding interactions. Further studies are warranted to validate and understand the binding capabilities of these compounds. Fig. 6 illustrates the presumed 2D and 3D binding modes of compound TAJ1 against NEK9.

For the TP53 protein, TAJ1 demonstrates a docking score of −9.5 kcal mol^{-1}, indicating strong binding affinity. The hydrogen bonding residue involved is ARG203, while the hydrophobic interactions occur with TYR92, LEU125, ALA200,

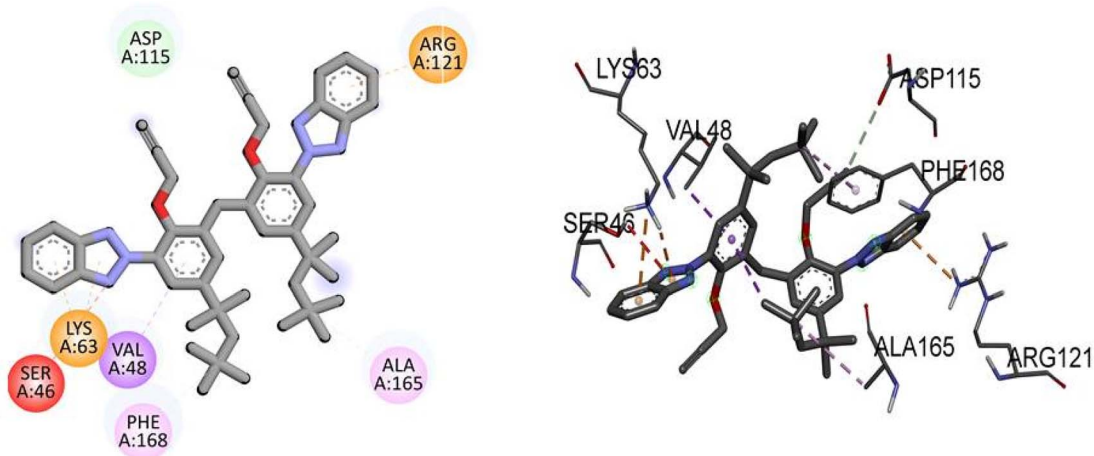

Fig. 5 The predicted 2D and 3D binding modes of TAJ1 against NEK7.

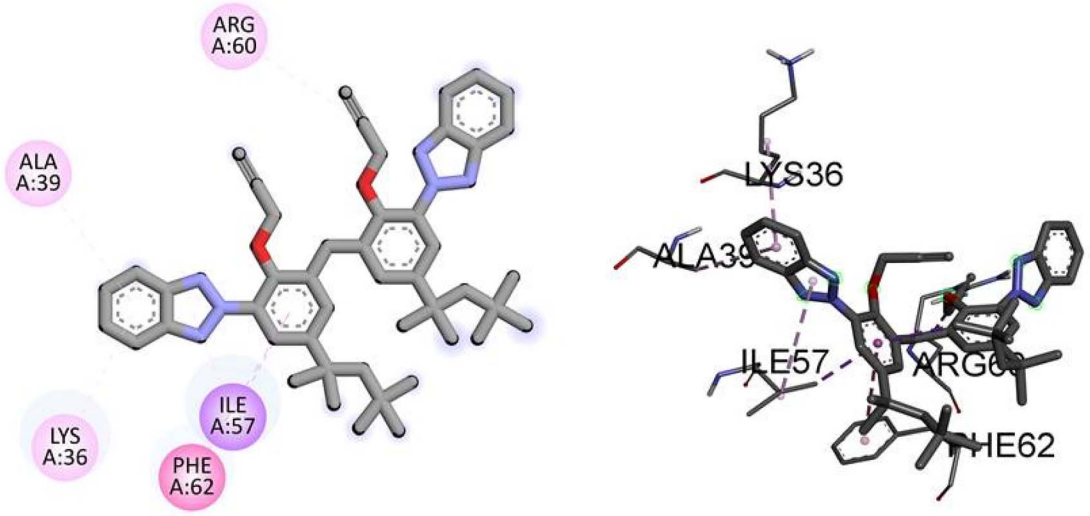

Fig. 6 The predicted 2D and 3D binding modes of TAJ1 against NEK9.

PRO115, ARG10, THR230, PRO231, and VAL229. These interactions suggest stable binding between TAJ1 and TP53. On the other hand, dabrafenib shows a docking score of −0.7 kcal-mol^{-1}, implying a weaker binding affinity. No specific hydrogen bonding residues or hydrophobic interactions are reported for dabrafenib. Fig. 7 illustrates the presumed 2D and 3D binding modes of compound TAJ1 against TP53.

Similarly, docking analysis showed the potent binding affinity of the synthesized compound and NF-KAPPA-B P65 with −8.8 kcal mol^{-1} binding energy, as given in Table 5. The predicted 2D and 3D binding modes of TAJ1 against NF-KAPPA are shown in Fig. 8. There is no conventional hydrogen bond between the amino acid residues and the protein molecule. Amino acid residue GLU103 forms pi-cation, VAL97 and ARG166 pi-sigma, while rest of the residues including PHE103, LEU89, VAL93, PHE77, and PRO69 develop alkyl and pi-alkyl linkages.

For caspase-3, TAJ1 shows a docking score of −7.3 kcal-mol^{-1}, indicating a moderate binding affinity. No specific hydrogen bonding residues are mentioned, but hydrophobic interactions occur with TRP206, TRY204, LEU168, and PHE256. These interactions contribute to the stability of the binding between TAJ1 and caspase-3. Dabrafenib, on the other hand, exhibits a docking score of −5.5 kcal mol^{-1}. It forms hydrogen bonds with LYS138, ASP146, and ARG147 residues, while no hydrophobic interactions are reported. Fig. 9 illustrates the presumed 2D and 3D binding modes of compound TAJ1 against caspase-3.

These findings provide insights into the potential binding modes and interactions of TAJ1 and dabrafenib with TP53, NF-

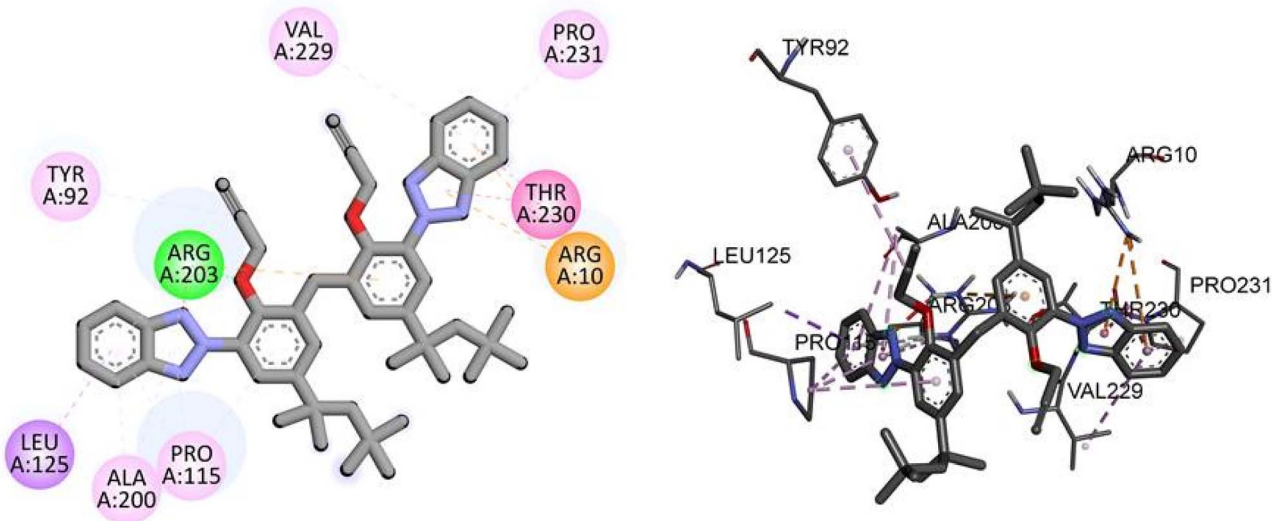

Fig. 7 The predicted 2D and 3D binding modes of TAJ1 against TP53.

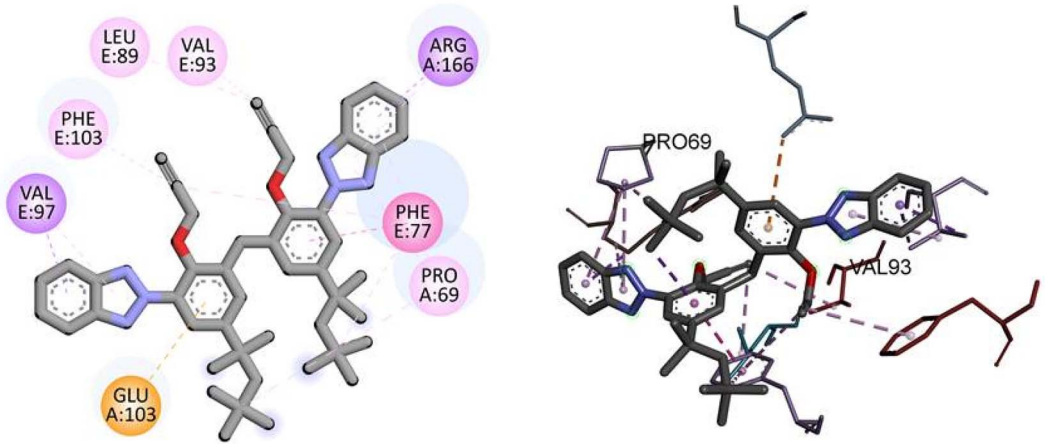

Fig. 8 The predicted 2D and 3D binding modes of TAJ1 against NF-KAPPA.

KAPPA-B, and caspase-3 proteins. However, it is important to note that these results are based on docking simulations, and further experimental validation is necessary to confirm the actual binding capabilities of these compounds with the respective proteins.

Molecular dynamic simulations. Replica MD simulations studies were performed to enhance the reliability and accuracy of the result. However, the main production run is given in main manuscript while the replica is given in the ESI (Fig. S8).† These simulations were employed to analyze the conformational stability of the apo protein and protein–ligand complex. To analyze the simulation results, root means square deviation (RMSD) and root mean square fluctuation of the apo protein, ligand and protein-ligand complex was calculated over time. From Fig. 10A, the RMSD of NEK2 can be predicted, and the analysis showed that the protein–ligand complex is more stable than the apo-protein or ligand. Initially, complex seemed to be stable to 24 ns; after that it attains more stability to 32 ns. At the end, the equilibrium is disturbed due to conformational changes in amino acid residues and the ligand molecule over 300 K. It is evident from Fig. 10A that the ligand–protein complex demonstrated significant conformational stability throughout the simulation, with an average root-mean-square deviation (RMSD) value of 2.96 Å. Remarkably, the apo protein molecule displayed the highest stability under the given conditions, as indicated by an average RMSD value of 3.01 Å. Conversely, the ligand TAJ1 molecule exhibited an average RMSD of 2.05 Å, indicating its relatively stable conformation throughout the simulation. These RMSD values collectively suggest that the system remained well equilibrated and maintained structural integrity throughout the simulation timeframe, compared to the RMSD of TP53 and NEK7. As given in Fig. 10B, the TAJ1-TP53 complex possesses an average RMSD of 4.76 Å higher than the NEK2 complex. Moreover, it is evident from Fig. 10C that the TAJ1-NEK7 complex exhibits an RMSD 2.48 Å lower than the NEK2 complex but possesses a higher degree of instability.

To analyze the flexibility of each residue, the RMSF was calculated and is shown in Fig. 10D, The RMSF average value of 0.94 Å suggests that amino acid residues were stable and exhibit

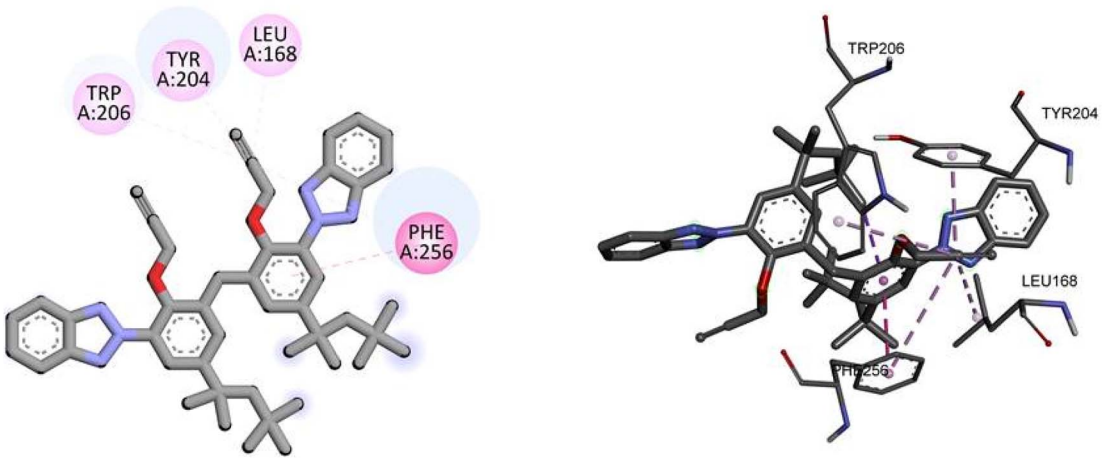

Fig. 9 The predicted 2D and 3D binding modes of TAJ1 against caspase-3.

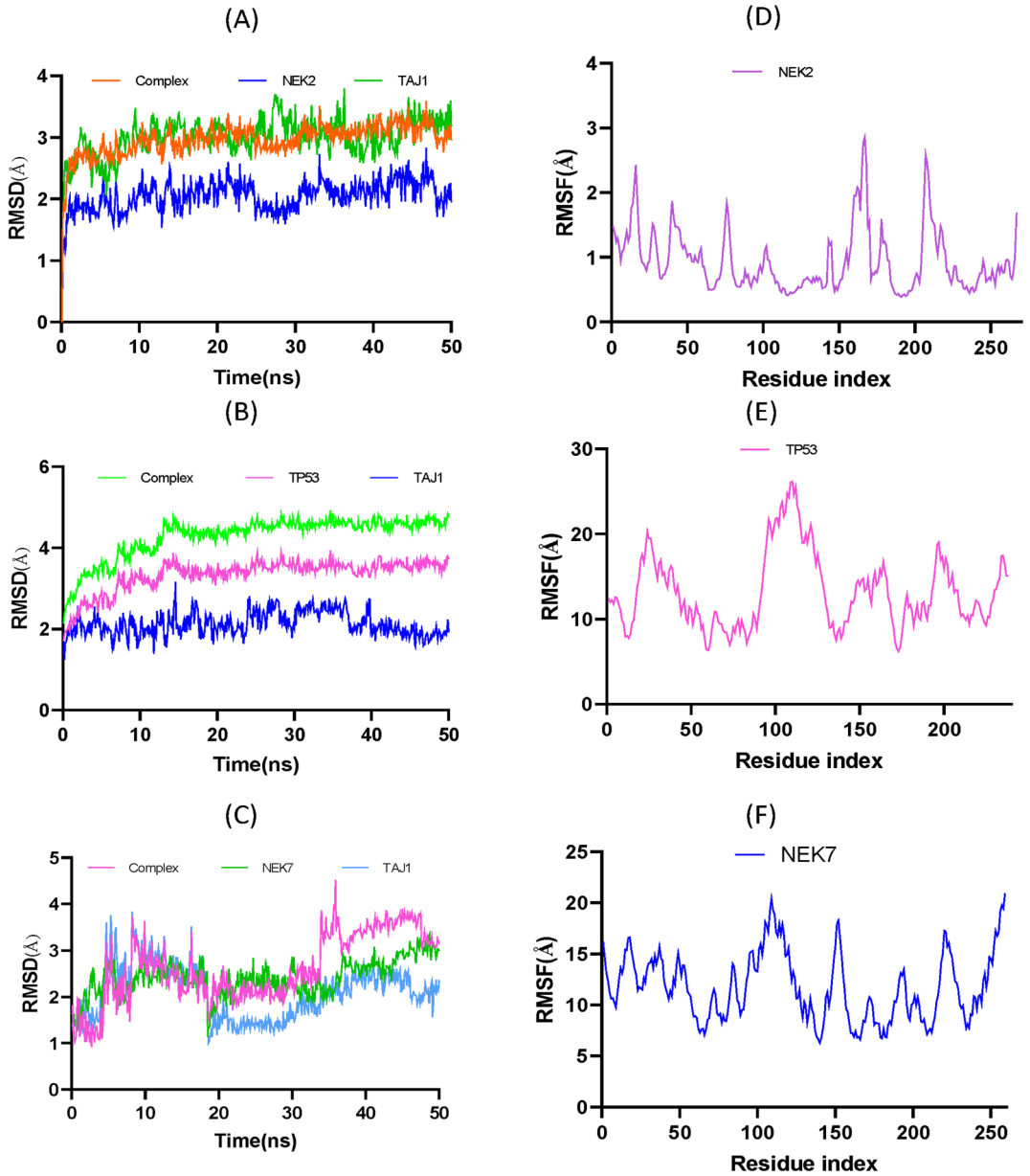

Fig. 10 (A) RMSD trajectories of TAJ1, NEK2 and their protein–ligand complex. (B) RMSD trajectories of TAJ1, TP53 and their protein–ligand complex. (C) RMSD trajectories of TAJ1, NEK7 and their protein–ligand complex. (D) RMSF trajectory of NEK2 showing the flexibility of the proteins. (E) RMSF trajectory of TP53 showing the flexibility of the proteins. (F) RMSF trajectory of NEK7 showing the flexibility of the proteins, which supports the potent ligand–protein interactions.

low oscillation. It is evident that the ligand was confined within the active pocket of the protein throughout the simulation time; however the nature of the interaction varies over time. The peaks in Fig. 10D show that residues have high vibrational oscillation, while the valleys show that ligand molecule interact with residues by strong hydrophobic and hydrophilic interactions. However, Fig. 10E exhibits the RMSF plot of TP53. The analysis showed that TP53 protein was found to be more flexible than NEK2. Similarly, at 300 K, the RMSF of NEK7 protein exhibits fluctuations resulting in NEK7 instability, as shown in Fig. 10F.

The intricate electrostatic interactions between the ligand molecule TAJ1 and the NEK2 protein can be elucidated by analyzing the amino acid residues involved in hydrogen bond formation. Upon examining Table 6, a fascinating analysis emerges, emphasizing the crucial role of specific NEK2, NEK7 and TP53 residues in establishing a robust hydrogen bond network with the ligand. Particularly noteworthy are the amino acid residues GLN187, LYS143, ARG164, and TYR193, which exhibit remarkable affinity for developing hydrogen bonds with the ligand's side atoms.

This exquisite interaction pattern contributes to the formation of a finely stable protein–ligand complex, as depicted with stunning clarity in Fig. 11. The distribution of hydrogen bond dynamics within the system unveils the capacity for bond formation and breakage throughout the simulation trajectory,

Table 6 Hydrogen bond donor and acceptor groups of TAJ1 against TP53, NEK2 and NEK7 protein

Sr #	Hydrogen bond donor	Hydrogen bond acceptor
NEK2-TAJ1 complex		
1	GLN187-side	TAJ1-side
2	LYS143-side	TAJ1-side
3	ARG164-side	TAJ1-side
4	TYR193-side	TAJ1-side
TP53-TAJ1 complex		
1	TAJ1-side	TYR92-side
2	ARG203-side	TAJ1-side
3	GLN23-main	TAJ1-side
4	SER228-side	TAJ1-side
5	ASN17-side	TAJ1-side
6	TAJ1-side	SER228-main
7	TAJ1-side	ILE21-main
NEK7-Taj1 complex		
1	TAJ1-side	ASP179-side
2	TAJ1-side	ASP118-side

encapsulating the ebb and flow of molecular interactions. This insightful exploration of hydrogen bond fluctuations not only unravels the intricate stability of the system but also offers captivating glimpses into the profound interplay between the ligand and protein, ultimately enriching our understanding of the dynamic forces governing their interaction.

The solvent accessible surface area (SASA) and radius of gyration (R_g) analysis provide insights into the conformational changes and structural stability of the apo protein molecule. In Fig. 12A the SASA analysis of NEK2 peaks indicates regions of the protein that are more exposed to solvent molecules, suggesting that these regions have a higher degree of flexibility and are not tightly packed. These exposed regions may undergo conformational changes as the protein progresses, potentially playing a role in the protein's function and interaction with other molecules. On the other hand, valleys in the SASA plot suggest buried residues that are tightly packed and have limited exposure to solvent. These regions are typically involved in the stability and folding of the protein, as they form the core structure of the molecule. Similarly, in Fig. 12B the SASA plot of TP53 exhibits greater stability of the protein compared to the SASA plot of NEK7 shown in Fig. 12C. It can be concluded that TP53 has a more compact structure than NEK2 or NEK7.

The Rg analysis in Fig. 12D provides information about the compactness of the protein conformation. Trough regions in the R_g plot indicate periods where the protein adopts a more globular, well-folded conformation. These regions correspond to stable conformations of the apo protein, where the residues are packed closely together, maintaining a compact structure. On the other hand, crest regions in the R_g plot suggest distorted conformations with more flexible regions of the protein. These crest regions may represent regions that are less stable or undergo conformational changes, leading to increased flexibility and a more expanded structure.

By combining the information from both the SASA analysis and the R_g analysis, you can shed light on how the conformation and stability of the apo protein molecule change over time or under different conditions. These analyses help in understanding the structure–function relationship of biomolecules and provide valuable information for studying protein dynamics and stability.

PCA (principal component analysis) and Pearson correlation are both valuable tools in the analysis of molecular dynamics (MD) simulations. PCA is commonly used in MD simulations to reduce the dimensionality of complex datasets and extract the most important features or motions. By identifying the principal components that capture the most significant variations in the data, PCA helps researchers gain insights into the essential modes of motion and understand the underlying dynamics of the system. Combining PCA and Pearson correlation provides a comprehensive understanding of the dynamics and relationships within MD simulations. This integrated approach allows for the identification of key motions, the exploration of correlated motions, and an assessment of relationships between different properties, contributing to a deeper understanding of the system under investigation. Fig. 13 illustrates the PCA analysis of all three complexes.

In the context of MD simulations, Pearson correlation can be employed to analyze the relationships between different structural or dynamic properties of biomolecules. For example, it can be used to examine the correlation between the fluctuations of different residues or domains, providing insights into the concerted motions and functional dynamics of the system.

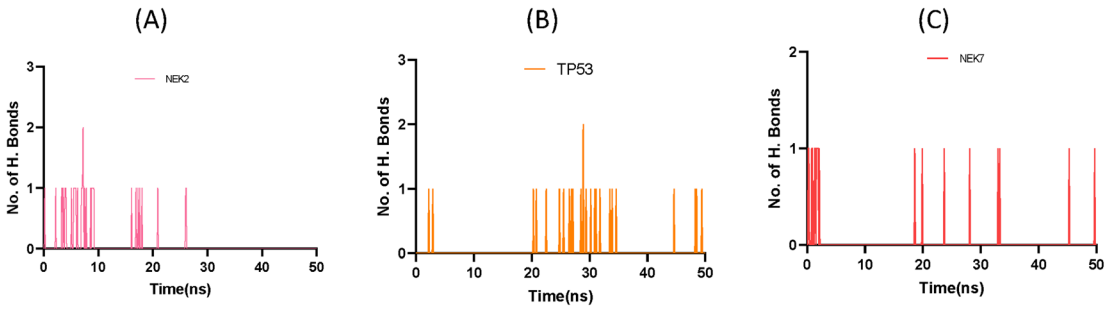

Fig. 11 Plot representing number of hydrogen bond interactions of NEK2 (A), TP53 (B) and NEK7 (C) protein during MD simulation.

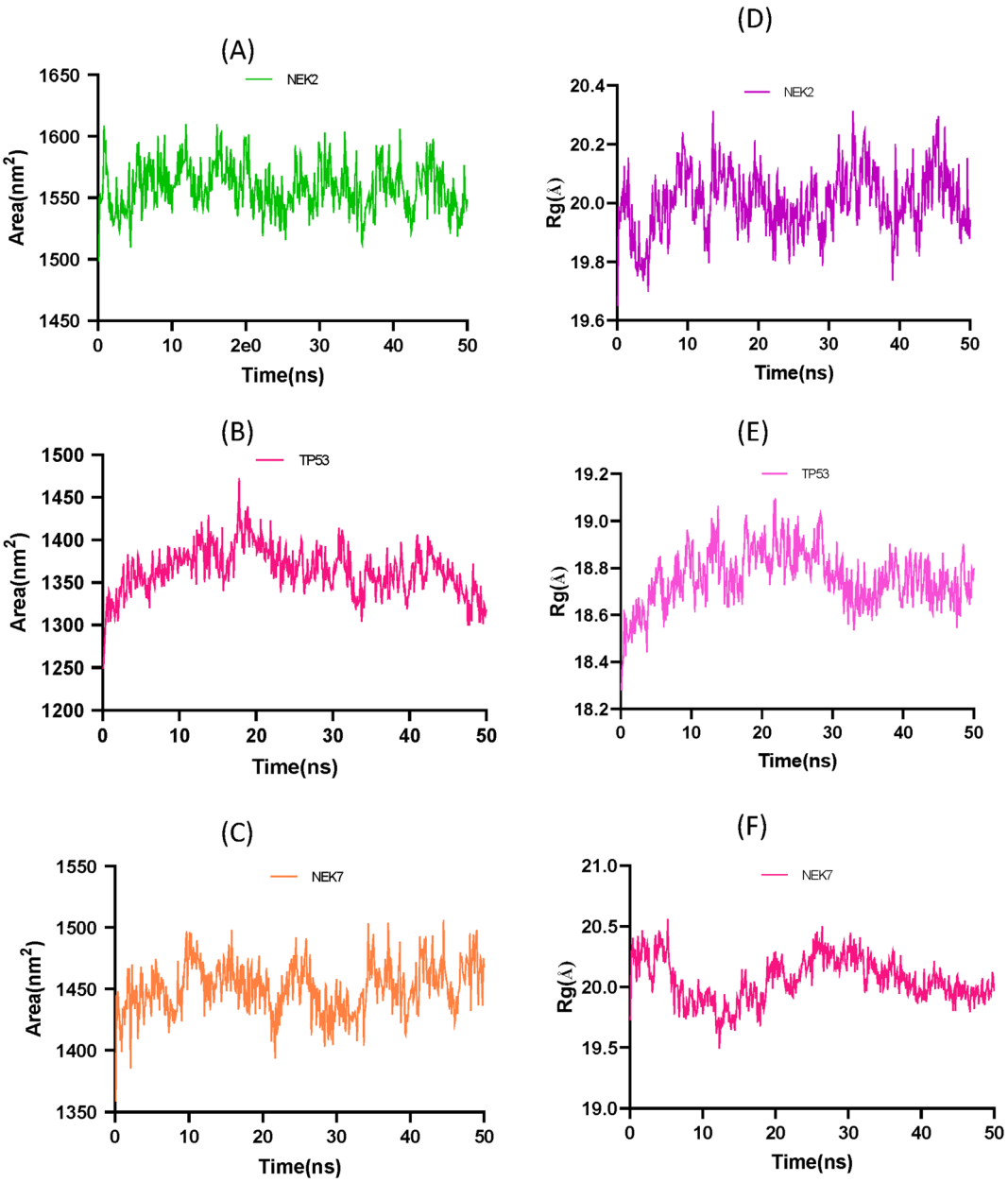

Fig. 12 (A) Solvent accessible surface area (SASA) plot of NEK2 protein over time. (B) Solvent accessible surface area (SASA) trajectory of TP53 protein over time. (C) Solvent accessible surface area (SASA) trajectory of NEK7. (D) Radius of gyration (R_g) trajectory of NEK2 protein over time. (E) Radius of gyration (R_g) trajectory of apo protein TP53. (F) Radius of gyration (R_g) trajectory of NEK7 protein over time.

Pearson correlation can also be used to assess the correlation between different properties, such as the correlation between protein flexibility and ligand binding affinity. PCA and Pearson correlation can be used together to enhance the analysis of MD simulations. PCA can be applied to reduce the dimensionality of the data and identify the most relevant variables or principal components. Subsequently, Pearson correlation can be used to analyze the relationships between these reduced variables or principal components, providing insights into the correlated motions or interactions within the system. Fig. 14 demonstrates the Pearson correlation of NEK2, NEK7 and TP53.

Free binding energy calculations (MMGBSA/MMPBSA)

Molecular dynamics simulations are widely used for studying protein–ligand interactions, and the accurate calculation of binding affinities and the free energy landscapes is crucial. Two commonly employed methods for this purpose are the molecular mechanics/Poisson–Boltzmann surface area (MMPBSA) and molecular mechanics/generalized Born surface area (MMGBSA) approaches. The MMPBSA method combines molecular mechanics calculations with Poisson–Boltzmann

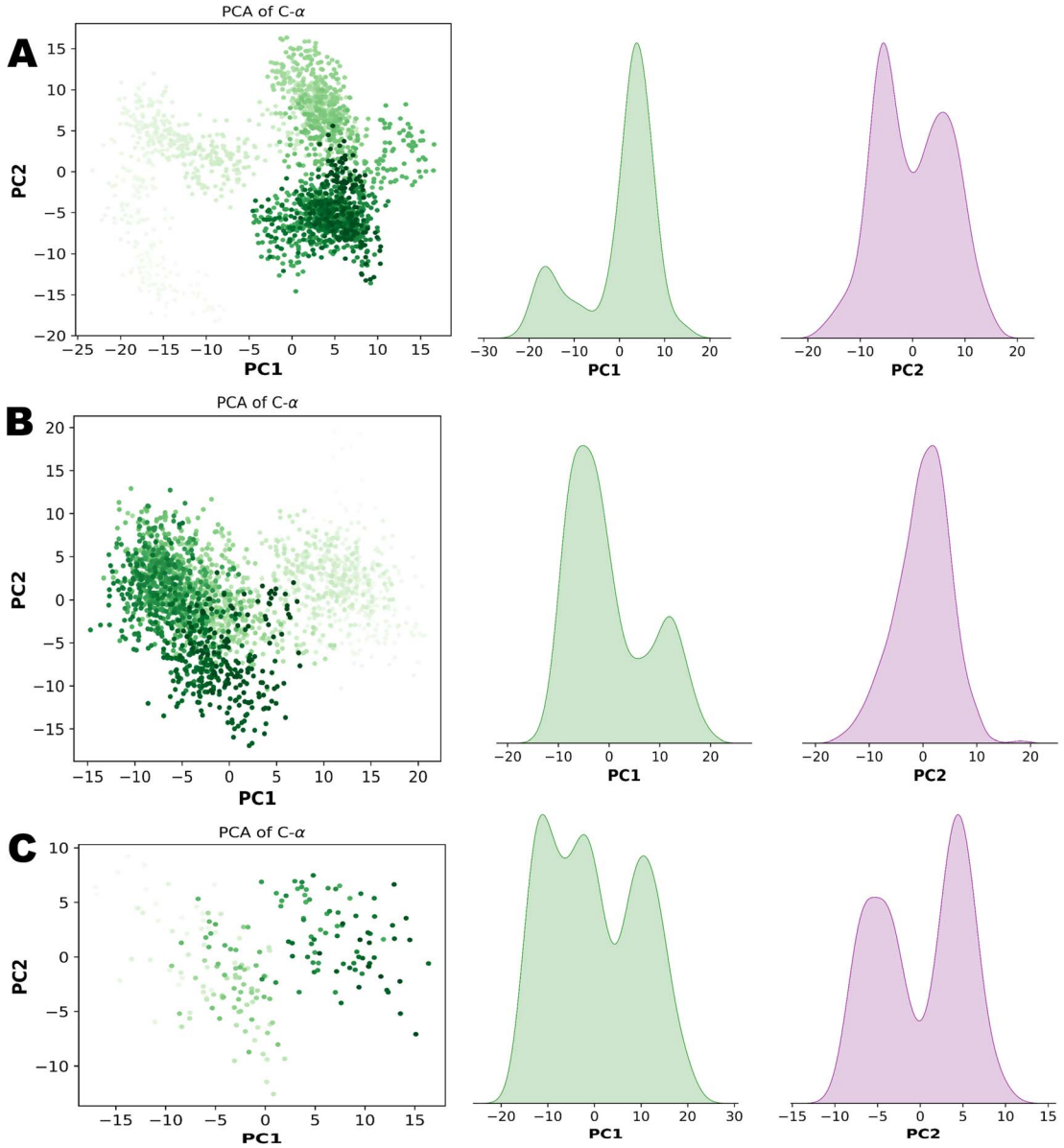

Fig. 13 (A) Principal component analysis of NEK2. (B) Principal component analysis of NEK7. (C) Principal component analysis of TP53.

and surface area terms, involving molecular dynamics simulation, energy calculation, and free energy calculation. The energy calculation decomposes the system's total energy into different components, while the free energy calculation uses the Poisson–Boltzmann equation and surface area term to account for solvation energies. In contrast, MMGBSA employs the

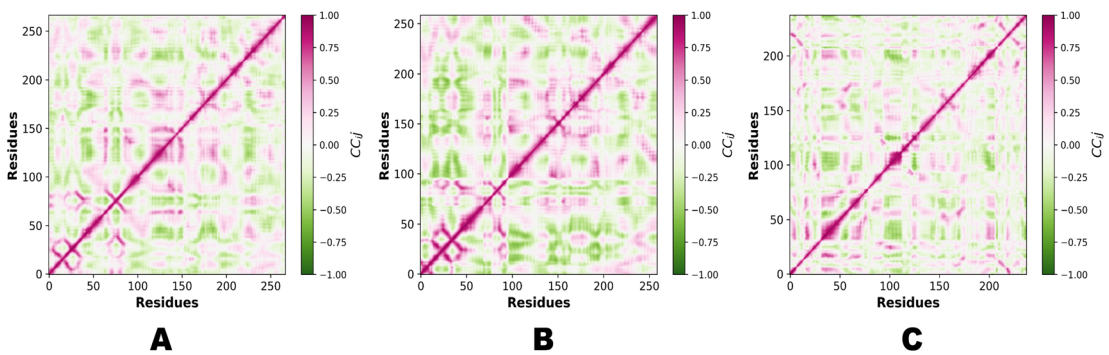

Fig. 14 (A) Pearson correlation of NEK2. (B) Pearson correlation of NEK7. (C) Pearson correlation of TP53.

Table 7 MMGBSA and MMPBSA analyses of simulated complexes

Complex	VDWAALS (kcal mol^{-1})	E_{EL} (kcal mol^{-1})	E_{GB} (kcal mol^{-1})	E_{SURF} (kcal mol^{-1})	Gibbs free energy (ΔG kcal mol^{-1})
NEK7-TAJ1 complex	−55.8287	−8.4647	33.979	−7.2579	−37.5722
NEK2-TAJ1 complex	−83.2802	−21.2883	50.4218	−9.1075	−63.2542
TP53-TAJ1 complex	−80.6956	−22.5581	47.3451	−9.2963	−65.2049

Complexes	VDWAALS (kcal mol^{-1})	E_{EL} (kcal mol^{-1})	E_{PB}	EN_{POLAR}	E_{DISPER}	Gibbs free energy (ΔG kcal mol^{-1})
NEK7-TAJ1 complex	−83.2802	−21.2883	63.453	−53.8014	97.1305	2.2136
NEK2-TAJ1 complex	−55.8287	−8.4647	46.176	−39.9491	72.9081	14.8416
TP53-TAJ1 complex	−80.6956	−22.5581	63.895	−55.7848	96.7935	1.6499

generalized Born approximation and involves the same three steps as MMPBSA. However, MMGBSA uses the generalized Born model to estimate solvation energy, making it computationally less expensive and suitable for larger systems. While MMPBSA is known for its accuracy in capturing electrostatics and solvation effects, MMGBSA is preferred for high-throughput virtual screening due to its computational efficiency. Ultimately, the choice between MMPBSA and MMGBSA depends on the specific research goals and system characteristics, with MMPBSA offering higher accuracy but at a higher computational cost, while MMGBSA provides a more efficient approach for larger systems. In the current study, both approaches were utilized to estimate the free binding energies observed during MD simulations for all complexes. Poisson–Boltzmann calculations were performed using an internal PBSA solver in mmpbsa_py_energy, whereas the generalized Born ESURF was calculated using LCPO surface areas. Table 7 provides the MMGBSA and MMPBSA free energy calculations of all complexes.

Conclusions

The benzotriazole derivative bis(3-(2*H*-benzo[*d*][1,2,3]triazol-2-yl)-2-(prop-2-yn-1-yloxy)-5-(2,4,4-trimethylpentan-2-yl)phenyl) methane (TAJ1) was synthesized and its inhibition potential against various proteins was predicted by *in silico* studies. XRD analysis confirmed the structure of the synthesized compound, showing that it possesses two aromatic parts linked *via* a CH_2 carbon with a bond angle of 108.40°. Density functional theory (DFT) calculations were performed to analyze the HOMO–LUMO analysis and global chemical reactivity descriptors of TAJ1. The HOMO–LUMO energy gap was determined to assess the molecule's chemical reactivity and stability. The compound exhibited a HOMO energy of −0.224 eV, a LUMO energy of −0.065 eV, and a HOMO–LUMO gap of 0.159 eV. Molecular docking analysis was conducted to evaluate the binding affinities of TAJ1 with various proteins. The compound showed potent interactions with NEK2, NEK7, NEK9, TP53, NF-KAPPA-B, and caspase-3 proteins, indicating its potential as a therapeutic agent. The binding energies and interacting amino acid residues were analyzed for each protein. Furthermore, MD simulation studies showed that the stability of these interactions is crucial because it ensures that compound TAJ1 remains tightly bound to the target proteins, increasing its potency as a therapeutic agent. By forming stable interactions with the active pocket, compound TAJ1 effectively inhibits the activity of NEK2, NEK7, NEK9, TP53, NF-KAPPA-B and caspase-3 which are known to play critical roles in cancer progression. Overall, these molecular dynamic simulation studies provide compelling evidence that compound TAJ1 has the ability to develop stable interactions with the active pocket regions of NEK2, suggesting its potential as a promising therapeutic agent for the treatment of cancer. The importance of hydrogen bonds in the studied system has been further confirmed, consolidating their significance. Despite existing limitations in the simulation methodology, we meticulously addressed these factors to guarantee the reliability of our results. Compound TAJ1 exhibits promising potential for optimization as a therapeutic agent targeting NEK2. These findings make a substantial contribution to the current understanding and create a pathway for the future development of highly effective and innovative anticancer treatments.

Author's contribution

Supervision and conceptualization: Syeda Abida Ejaz and Mubashir Aziz, data analysis; Mubashir Aziz, Tahir Qadri and Pervaiz Ali Channar, data curation: Mumtaz Hussain, Zahid Hussain, Hafiz Muhammad Attaullah and Rabial Ujan, writing original draft and validation; Tasneem Zehra, Aamer saeed and M. R. Shah. resources; Hanan A. Ogaly, and Fatimah AM Al-Zahrani.

Conflicts of interest

The authors declare no conflict of interest.

Acknowledgements

The authors are thankful to Deanship of Scientific Research (DSR), King Khalid University, Abha, Saudi Arabia, for facilitating research activities under Research Grant no. RGP.2/93/44.

References

1 M. Aziz, S. A. Ejaz, S. Zargar, N. Akhtar, A. T. Aborode, T. A. Wani, G. E.-S. Batiha, F. Siddique, M. Alqarni and A. A. Akintola, *Molecules*, 2022, **27**, 4098.

2 o. a. c. d. w.**https://www.cancerresearchuk.org/health-professional/cancer-statistics/worldwide-cancer#:~:text=Therewere18.1millionnew**.

3 A. Sokolova, K. Johnstone, A. McCart Reed, P. Simpson and S. Lakhani, *Histopathology*, 2023, **82**(1), 70–82.

4 Z. Sun, W. Gong, Y. Zhang and Z. Jia, *Front. physiol.*, 2020, **11**, 606996.

5 R. Tan, S. Nakajima, Q. Wang, H. Sun, J. Xue, J. Wu, S. Hellwig, X. Zeng, N. A. Yates and T. E. Smithgall, *Mol. Cell*, 2017, **65**, 818–831.

6 T. Haq, M. W. Richards, S. G. Burgess, P. Gallego, S. Yeoh, L. O'Regan, D. Reverter, J. Roig, A. M. Fry and R. Bayliss, *Nat. Commun.*, 2015, **6**, 8771.

7 D. G. Hayward and A. M. Fry, *Cancer Lett.*, 2006, **237**, 155–166.

8 A. M. Fry, L. Arnaud and E. A. Nigg, *J. Biol. Chem.*, 1999, **274**, 16304–16310.

9 R. S. Hames and A. M. Fry, *Biochem. J.*, 2002, **361**, 77–85.

10 D. G. Hayward, R. B. Clarke, A. J. Faragher, M. R. Pillai, I. M. Hagan and A. M. Fry, *Cancer Res.*, 2004, **64**, 7370–7376.

11 N. Tsunoda, T. Kokuryo, K. Oda, T. Senga, Y. Yokoyama, M. Nagino, Y. Nimura and M. Hamaguchi, *Cancer Sci.*, 2009, **100**, 111–116.

12 A. M. Fry, R. Bayliss and J. Roig, *Front. Cell Dev. Biol.*, 2017, **5**, 102.

13 F. Van Hauwermeiren and M. Lamkanfi, *Nat. Immunol.*, 2016, **17**, 223–224.

14 Z. Xu, W. Shen, A. Pan, F. Sun, J. Zhang, P. Gao and L. Li, *Pathology*, 2020, **52**, 329–335.

15 Y. Kaneta and A. Ullrich, *Biochem. Biophys. Res. Commun.*, 2013, **442**, 139–146.

16 M. Aziz, S. A. Ejaz, N. Tamam, F. Siddique, N. Riaz, F. A. Qais, S. Chtita and J. Iqbal, *Sci. Rep.*, 2022, **12**, 6404.

17 T. A. Jimoh, A. O. Oyewale, H. Ibrahim, J. D. Habila and D. E. Arthur, *Chem. Afr.*, 2022, **5**, 509–523.

18 J. H. Xu, Y. L. Fan and J. Zhou, *J. Heterocycl. Chem.*, 2018, **55**, 1854–1862.

19 Y. Chen, Y. Liu, Y. Xie, H. Zhang, X. Du and Z. J. J. O. A. Zhang, *J. Alloys Compd.*, 2022, **893**, 162305.

20 A. R. Katritzky, S. Rachwal and G. J. Hitchings, *Tetrahedron*, 1991, **47**, 2683–2732.

21 E. Loukopoulos and G. E. Kostakis, *Coord. Chem. Rev.*, 2019, **395**, 193–229.

22 H. B. Bollikolla, S. M. Boddapati, S. Thangamani, B. R. Mutchu, M. M. Alam, M. Hussien and S. B. Jonnalagadda, *J. Heterocycl. Chem.*, 2023, **60**, 705–742.

23 K. M. Dawood, H. Abdel-Gawad, E. A. Rageb, M. Ellithey and H. A. J. B. Mohamed, *Bioorg. Med. Chem.*, 2006, **14**, 3672–3680.

24 K. Kopańska, A. Najda, J. Żebrowska, L. Chomicz, J. Piekarczyk, P. Myjak and M. J. B. Bretner, *Bioorg. Med. Chem.*, 2004, **12**, 2617–2624.

25 A. R. Dwivedi, S. S. Rawat, V. Kumar, N. Kumar, R. Yadav, S. Barnwal, A. Prasad and V. Kumar, *Bioorg. Med. Chem.*, 2022, **72**, 116976–116990.

26 S. Y. Alraqa, K. Alharbi, A. Aljuhani, N. Rezki, M. R. Aouad and I. Ali, *J. Mol. Struct.*, 2020, **1225**, 129192.

27 R. Ibba, S. Piras, P. Corona, F. Riu, R. Loddo, I. Delogu, G. Collu, G. Sanna, P. Caria and T. Dettori, *Front. Chem.*, 2021, **9**, 327.

28 G. H. LeFevre, A. Lipsky, K. C. Hyland, A. C. Blaine, C. P. Higgins and R. G. Luthy, *Environ. Sci.: Water Res. Technol.*, 2017, **3**, 213–223.

29 S. D. Khalaf, N. A. A.-S. Ahmed and A. H. Dalaf, *Mater. Today: Proc.*, 2021, **47**, 6201–6210.

30 I. Briguglio, S. Piras, P. Corona, E. Gavini, M. Nieddu, G. Boatto and A. Carta, *Eur. J. Med. Chem.*, 2015, **97**, 612–648.

31 A. R. Katritzky and B. V. Rogovoy, *Chem. Eur. J.*, 2003, **9**, 4586–4593.

32 X.-L. Tang, W. Dou, J.-a. Zhou, G.-L. Zhang, W.-S. Liu, L.-Z. Yang and Y.-L. Shao, *CrystEngComm*, 2011, **13**, 2890–2898.

33 H. A. El-Asmy, I. S. Butler, Z. S. Mouhri, B. J. Jean-Claude, M. S. Emmam and S. I. Mostafa, *J. Mol. Struct.*, 2014, **1059**, 193–201.

34 I. Briguglio, S. Piras, P. Corona, E. Gavini, M. Nieddu, G. Boatto and A. Carta, *Eur. J. Med. Chem.*, 2015, **97**, 612.

35 Y. Wang, Y. Li, Y. Fan, Z. Wang and Y. J. C. C. Tang, *Chem. Commun.*, 2017, **53**, 11873–11876.

36 S. Talukdar, R.-J. Chen, C.-T. Chen, L.-C. Lo and J.-M. Fang, *J. Comb. Chem.*, 2001, **3**, 341–345.

37 T. Mosmann, *J. Immunol. Methods*, 1983, **65**, 55–63.

38 M. Niks, *J. Immunol. Methods*, 1990, **130**, 149–151.

39 J. Iqbal, S. A. Ejaz, A. Saeed and M. Al-Rashida, *Eur. J. Pharmacol.*, 2018, **832**, 11–24.

40 N. Sebbar, M. Ellouz, E. Essassi, Y. Ouzidan and J. Mague, *Acta Crystallogr., Sect. E: Crystallogr. Commun.*, 2015, **71**, o999.

41 N. Ž. Janković, S. M. Stefanović, J. Petronijević, N. Joksimović, S. B. Novaković, G. A. Bogdanović, J. Muškinja, M. Vraneš, Z. R. Ratković and Z. M. Bugarčić, *ACS Sustain. Chem. Eng.*, 2018, **6**, 13358–13366.

42 A. L. Spek, *Acta Crystallogr., Sect. D: Biol. Crystallogr.*, 2009, **65**, 148–155.

43 F. L. Hirshfeld, *Theor. Chim. Acta*, 1977, **44**, 129–138.

44 M. A. Spackman and D. Jayatilaka, *CrystEngComm*, 2009, **11**, 19–32.

45 P. R. Spackman, M. J. Turner, J. J. McKinnon, S. K. Wolff, D. J. Grimwood, D. Jayatilaka and M. A. Spackman, *J. Appl. Crystallogr.*, 2021, **54**, 1006–1011.

46 U. Vanitha, R. Elancheran, V. Manikandan, S. Kabilan and K. Krishnasamy, *J. Mol. Struct.*, 2021, **1246**, 131212.

47 K. Bhavani, S. Renuga and S. Muthu, *Spectrochim. Acta, Part A*, 2015, **136**, 1260–1268.

48 M. Aziz, S. A. Ejaz, B. A. Alsfouk, A. Sultan and C. Li, *Arch. Biochem. Biophys.*, 2023, **747**, 109761.

49 *R. A. Gaussian09, Inc.*, Wallingford CT, 2009, 121, 150–166.

50 F. Siddique, M. Langer, M. t. Paloncýová, M. Medved', M. Otyepka, D. Nachtigallová, H. Lischka and A. l. J. Aquino, *J. Phys. Chem. C*, 2020, **124**, 14327–14337.
51 R. Dennington, T. A. Keith and J. M. Millam, *GaussView, version 6.0. 16*, Semichem Inc., Shawnee Mission, KS, USA, 2016.
52 P. D. Bank, *Nat. Cell Biol.*, 1971, **233**, 223.
53 D. S. Goodsell, M. F. Sanner, A. J. Olson and S. Forli, *Protein Sci.*, 2021, **30**, 31–43.
54 T. Brown, *J. Sci. Teacher*, 2014, **81**, 67.
55 M. Amir, T. Mohammad, K. Prasad, G. M. Hasan, V. Kumar, R. Dohare, A. Islam, F. Ahmad and M. J. Imtaiyaz Hassan, *J. Biomol. Struct. Dyn.*, 2020, **38**, 4625–4634.
56 J. Lee, X. Cheng, J. M. Swails, M. S. Yeom, P. K. Eastman, J. A. Lemkul, S. Wei, J. Buckner, J. C. Jeong and Y. Qi, *J. Chem. Theory Comput.*, 2016, **12**, 405–413.
57 T. Hansson, C. Oostenbrink and W. van Gunsteren, *Curr. Opin. Struct. Biol.*, 2002, **12**, 190–196.
58 T. Qadri, I. Anis, M. Shah and S. W. Ng, *Acta Crystallogr., Sect. E: Struct. Rep. Online*, 2011, **67**, o738.